nature communications



Article

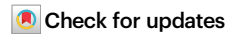
https://doi.org/10.1038/s41467-025-64463-2

Periodically-modulated unipolar and bipolar orders in nematic fluids towards miniaturized nonlinear vectorial optics

Received: 16 January 2025

Accepted: 15 September 2025

Published online: 24 October 2025



Guang-Yang Zhang^{1,2,3,4}, Ling-Ling Ma $^{f 0}$ ^{1,2,3,4} \boxtimes , Enjun Lin^{5,6,7,8}, Ze-Yu Wang^{1,2,3,4}, Jin-Tao Pan^{1,2,3,4}, Jidan Yang^{5,6,7,8,9}, Minghui Deng^{5,6,7,8}, Yang Wei^{1,2,3,4}, Yong Ye^{1,2,3,4}, Ning Wang^{1,2,3,4}, Yu Wang $^{f 0}$ ^{1,2,3,4} \boxtimes , Satoshi Aya $^{f 0}$ ^{5,6,7,8} \boxtimes & Yan-Qing Lu $^{f 0}$ ^{1,2,3,4} \boxtimes

Complex polar topological configurations are the foundation for exploring exotic phases and nontrivial emergent phenomena in condensed-matter physics. While numerous topological configurations like skyrmions and merons are known to occur spontaneously in various materials, achieving the designability of magnetically- and electrically-polar textures in a controlled manner is a long-standing challenge in domain engineering. Here, we discover an unprecedented mesophase that exhibits unipolar and bipolar orders, where both apolar and polar orientational order parameters are modulated. The polar state enables defect-free polar patterning with designability and controllability on large scales. A case study demonstrates the facile generation of second-harmonic perfect vector beams through photopatterned topological polar liquid crystal superstructures. Remarkably, this single-layer, micrometerthin-film device attains functionalities comparable to multiple conventional optical components, establishing a foundation for advanced nonlinear vectorial optics at the micrometer scale.

Topological states of polar matter are essential to determining the systems' electromagnetic and optical properties. Even in a particular thermodynamic phase, the topological nature, e.g., how a polar vectorized field orients in space, would dramatically revise phase behaviors. The spin colossal magnetoresistance effect represents an important example¹⁻³. The 'colossal' modulation of spin current is induced by the Néel vector and anisotropy of antiferromagnetic materials near the Néel temperature, which determines the transition between the insulating and conducting phases. Ferromagnetic

materials with skyrmion or meron lattices feature non-coplanar topological solitons, promising applications in information-carrying and high-density storage devices⁴⁻⁷. In the electrical counterpart, various ferroelectric flux-closures, vortices, meron, bubbles, polar waves, and hedgehog states were found, which lead to unusual phase transitions, topological behaviors, and unprecedented physical properties⁵. Even within the same phase, tailoring topological orders in polar materials can bring enticing possibilities and a generic strategy in exploring and even designing unprecedented properties that will lead

¹National Laboratory of Solid State Microstructures, Nanjing University, Nanjing, China. ²Key Laboratory of Intelligent Optical Sensing and Manipulation, Nanjing University, Nanjing, China. ³Collaborative Innovation Center of Advanced Microstructures, Nanjing University, Nanjing, China. ⁴College of Engineering and Applied Sciences, Nanjing University, Nanjing, China. ⁵South China Advanced Institute for Soft Matter Science and Technology (AISMST), South China University of Technology, Guangzhou, China. ⁵School of Emergent Soft Matter, South China University of Technology, Guangzhou, China. ⁷Guangdong Provincial Key Laboratory of Functional and Intelligent Hybrid Materials and Devices, South China University of Technology, Guangzhou, China. ⁸Guangdong Basic Research Center of Excellence for Energy and Information Polymer Materials, South China University of Technology, Guangzhou, China. ⁹Present address: College of Electronic and Optical Engineering & College of Flexible Electronics (Future Technology), Nanjing University of Posts and Telecommunications, Nanjing, China. ⊠e-mail: malingling@nju.edu.cn; yuwang87@nju.edu.cn; satoshiaya@scut.edu.cn; yqlu@nju.edu.cn

to exotic functionalities. However, the method of diversifying topological polar structures and controlling their spatial distribution is unestablished.

Traditional polar systems are typically solid-state with proper low symmetries, where the involved polar interactions are rather short-ranged with limited tunability in response to external fields. Recent studies have revealed that high-energy external fields can be used for achieving positional-dependent alignment of electrical dipoles, but with considerable limitations. For instance, high-field electrical poling was proposed to fabricate out-of-plane polar structures with simple up or/and down polarizations. This technique has enabled the commercialization of frequency-doubling devices based on the quasi-phase-matching mechanism^{8,9}. In 2008, femtosecond laser writing was shown to be a potential non-contact technique to implement the out-of-plane design of polarization field at optical precision¹⁰. While out-of-plane domain engineering is particularly useful in developing ferroelectric devices, the in-plane counterpart has been unrealized and is another critical dimension that would allow strong and direct electromagnetic interactions between polarizations of matter and electromagnetic waves.

Liquid crystals (LCs) are unique soft-matter states featuring anisotropy of quasi-long-ranged orderings and interactions at mesoscales, which can sensitively couple to different external stimuli¹¹⁻¹⁵. Selfassembly processes under distinct combinations of ordering and interactions to fields have the capability of forming diverse threedimensional topological structures 16-21 and have opened up new vistas to explore topological counterparts in optics²²⁻³⁰. One of the most wellstudied and industrial-valuable LCs is the nematic (N) LC, which is a three-dimensional fluid and possesses only partial orientational ordering with a head-to-tail equivalent nature (i.e., apolar). The nematic ordering has recently met the polar ordering, leading to various polar LC states, such as the ferroelectric nematic (NF) state³¹⁻³⁴. The inversion symmetry is broken therein, and large spontaneous polarization occurs³³. Unlike electrically-poled organic nonlinear materials produced by high external fields, the polar LC material group can self-build in-plane polar fields without unfavorable polarization relaxation, thereby providing an unprecedented opportunity to extend the realm of apolar topology to polar counterparts.

Numerous recent discoveries suggest that the unique combination of polar and nematic elastic interactions can dramatically diversify exotic polar structures unfamiliar to those in the traditional ferroelectric crystalline and LC systems^{35–37}. The complexity of interactions has generated considerable interest in condensed matter physics, but also exposes great challenges for developing defect-free/high-performance NF-LC electrooptic devices 34,36,38,39. This has been unobtainable primarily because of the intricate energy competitions (among elastic energy, Landau energy, polarization gradients, flexoelectricity, and electrostatics), which limit the fabrication of defect-free and highperformance polar structures^{36,38,39}. Here, we experimentally demonstrate that an unidentified polar nematic state, the Nx phase, emerges between the apolar N and NF phases. The Nx phase exhibits two types of polarization fields: (1) an unprecedented unipolar structure separated by periodic apolar regimes and (2) an alternating bipolar structure. Such a state of matter possesses both strong second-harmonic generation (SHG) activity and excellent controllability of the spatial distribution of polarizations. By employing photoalignment technology, defect-free in-plane domain engineering with considerable freedom of designability in the Nx phase is realized. In addition, we successfully generate second-harmonic perfect vector beams using a single device featuring a micrometer-thin LC layer, which performs the same functions as a large-scale optical system made up of multiple optical components. This work provides an excellent platform for engineering three-dimensional polar topological structures, which is promising for exploring emergent phenomena and exotic phases in condensed matter physics and nonlinear optical applications.

Results

Liquid-matter ferroelectrics with two distinct polar phases

We design a highly polar rod-like LC material, NJU001, that combines the structural features of the prototype NF materials of RM734 (Fig. 1a) and DIO (Fig. 1b), where a terminal nitro group is introduced at one end and a short methoxy chain at the other end. A fluorine atom and a trifluoromethyl group are attached as bulky side groups (Fig. 1c). The material synthesis flow is provided in Supplementary Section 1. The differential scanning calorimetry (DSC) thermograms indicate three distinct mesophases (N, Nx, and NF) upon cooling, with transition points at 132 °C ($\Delta H = 0.500 \text{ kJ mol}^{-1}$), 76 °C ($\Delta H = 0.009 \text{ kJ mol}^{-1}$) and 58 °C ($\Delta H = 0.216 \text{ kJ mol}^{-1}$), respectively (Fig. 1d and Supplementary Fig. S6). Polarized light microscopy (PLM) finds that, upon cooling, all the phases exhibit the nematic nature with structural evolution from a schieren N texture to a striped Nx texture and finally to a banded texture characteristic of the NF phase (Supplementary Fig. S7).

As complementary characterizations, the SHG (Fig. 1e) and the transient current (P-E loops) measurements upon a triangle-wave field application (Fig. 1f, g and Supplementary Fig. S8) are used to determine the polar nature of each phase. In the N phase, the materials show a seemingly inactive SH signal similar to the traditional apolar nematics. In the NF phase, a strong SH signal and current peak by a large peak per half period of the applied field are confirmed. Meanwhile, the Nx phase exhibits intermediate characteristics between the N and NF phases. In the high-temperature region of the Nx phase (70 ~ 76 °C), the SH signal is vanishingly small, but the finite spontaneous polarization grows continuously with decreasing temperature. This indicates that the polar order starts to develop from the apolar nematic background, but the cluster size of polar regions should be smaller than the probe wavelength $(\lambda = 1300 \text{ nm})$. As the temperature further decreases, say below 70 °C, an observable SH signal appears. The enhanced SH signal and parallelogram-shaped P-E loop (Fig. 1e and Supplementary Fig. S8) with decreasing temperature confirm that the polar regions are now at the macroscopic scale, larger than the optical wavelength. The nonlinear coefficient d_{33} is experimentally determined to be approximately 5.7 pm/V and 6.9 pm/V at 61.0°C (Nx) and 45.7°C (NF), respectively (Supplementary Section 2).

Unipolar and bipolar orders in the Nx phase

The gradual growth of the polar order in the Nx phase is characterized by two types of unique kinetic transitional pathways from the apolar nematic state (Fig. 2a-i). The first one, Pathway I, of forming periodically-modulated unipolar orders, similar to the concept of unipolar voltages with a single voltage referenced to zero volts, with alternative apolar regimes separating neighboring syn-polar regions (Fig. 2a-ii), is an unidentified nontrivial process where flexoelectricity plays an essential role as discussed later. PLM observations reveal that the texture of the unidirectionally aligned NJU001 material transitions from an isotropic state at 132 °C to a smooth N state and then to the Nx mesophase (Fig. 2b). The Nx stripes, as a similar texture to the splay nematic^{40,41}, appear along the direction of the nematic background. Small splay director distortions are evidenced in stripes using the PolScope (Supplementary Fig. S9). The contrast of the Nx stripes increases with decreasing temperature (Supplementary Fig. S10). The Nx stripes show spatially-modulated SH signal confirmed by SHG microscopy (Fig. 2c). It is worth noting that the appearance of SHGactivated Nx stripes does not depend on the polarization of the fundamental wave (FW; Fig. 2c and Supplementary Fig. S11a). Especially for the excitation with circular polarization, transitional dark regions between adjacent stripes show no SH signal (Supplementary Fig. S11a). This indicates that the transitional region corresponds to either a disclination or an apolar nematic region. The width of the stripes is approximately 2.4 µm at the cell gap of 4.0 µm, matching that of the Nx stripes in PLM images (Fig. 2b).

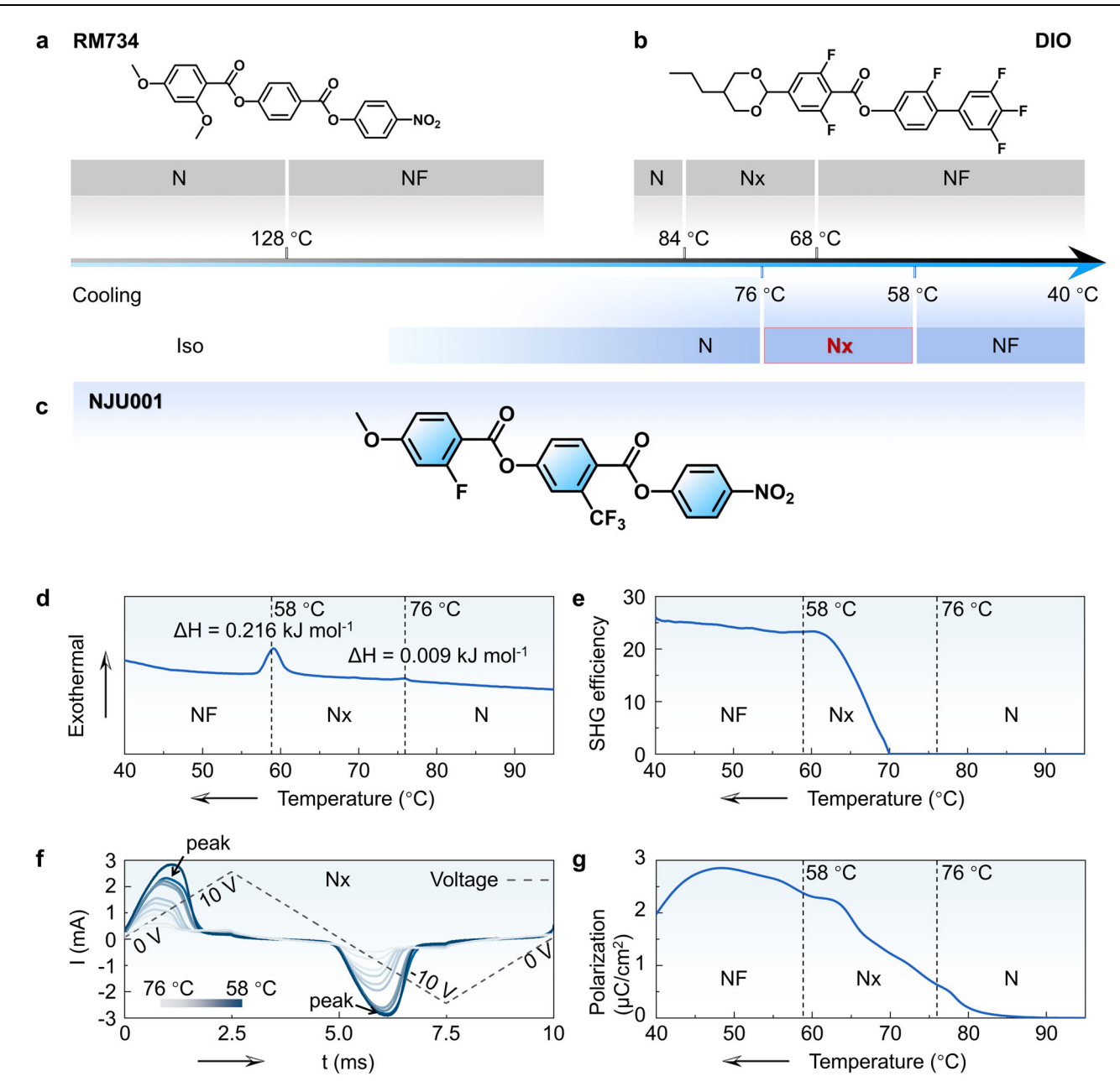


Fig. 1 | **Characterization of the polar nematic LC material. a-c** Chemical structures and phase behaviors of RM734, DIO, and NJU001 materials. N: nematic phase; NF: ferroelectric nematic phase. Iso: isotropic phase. **d** DSC of the NJU001 material during the cooling process at a scan rate of 5 K min⁻¹. **e** SHG efficiency of the NJU001 material as a function of the temperature. SHG efficiency is defined as the SHG intensity ratio of the NJU001 material to that of a Y-cut quartz plate. The thickness

of the Y-cut and NJU001 samples was 2 mm and 5.2 µm, respectively. The sample is unidirectionally photoaligned. SHG: second-harmonic generation. **f** Switching-current response of NJU001 material in the Nx phase under an applied triangular wave. **g** Temperature dependence of the spontaneous polarization curve. Source data are provided as a Source Data file.

As the SHG microscopy cannot determine the orientation of dipoles, we further employ SHG interferometry (SHG-I) microscopy³⁵ to image the polar field (Supplementary Fig. S12). The neighboring stripes exhibit syn-parallel alignment of polarizations, evidenced by the same optical phase of the interfered SH signals. Visually, the adjacent stripes (e.g., Stripe 1 and Stripe 2 in Fig. 2c) darken or brighten simultaneously upon varying the phase of the SH reference. Based on these findings, we first rule out the Ising, Néel, and Bloch models (Supplementary Section 3). These models are classical domain wall structures typically found in solid-state ferroelectrics and characterized by anti-polar domains with a domain wall in between. Considering the negligible SH signal detected in the transitional region between the adjacent stripes, we could arrive at two nontrivial Unipolar models. In

Unipolar model A, the transitional region between the stripes exhibits an apolar nematic nature. That is, the polar order vanishes, but the nematic orientational order remains (Fig. 2a-ii). In Unipolar model B, a typical domain wall, i.e., a disclination with an orientational disorder, separates the adjacent polar stripes (Supplementary Fig. S13). To identify which model is plausible, we examine the orientational anisotropy of the transitional region. By rotating the sample under PLM, both the stripes and the transitional region show the brightest state when the orientation of the stripes makes 45° off from one of the polarizers, and they become extinct when the orientation of the stripes is parallel to one of the polarizers (Supplementary Fig. S14a, b). The difference in brightness and the brightness variation between stripes and the transitional region is slight. This indicates that the transitional

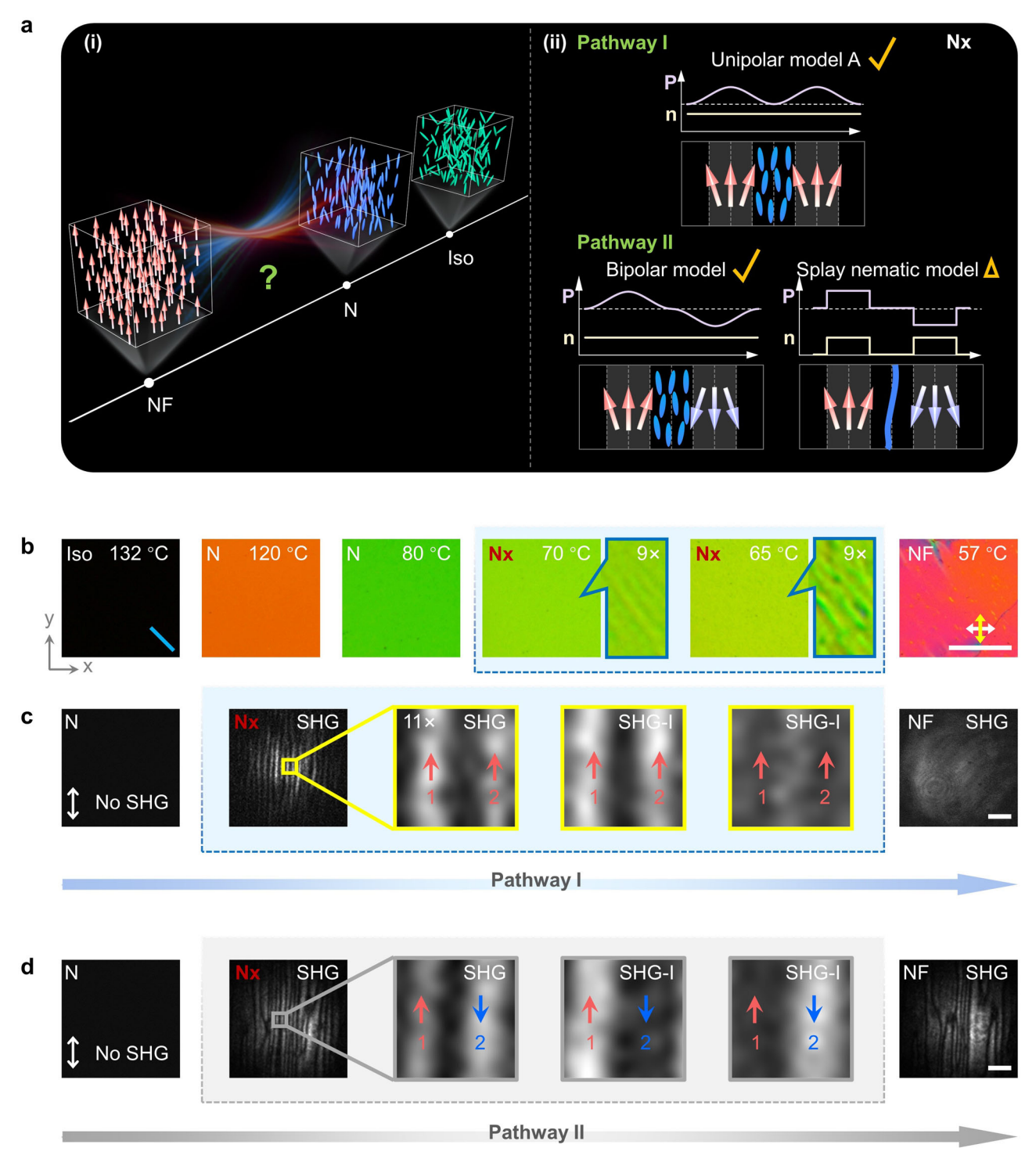


Fig. 2 | **Unipolar and bipolar orders of the Nx phase. a** (i) Schematic of the LC ordering evolution in different phases. (ii) Schematic of Unipolar model A, Bipolar model, and Splay nematic model for the Nx phase. **P** and **n** denote the parameters of polar and orientation ordering, respectively. N: nematic phase; NF: ferroelectric nematic phase. Iso: isotropic phase. **b** PLM texture evolution as the temperature decreases. The white and yellow arrows denote crossed polarizers. The blue bar represents the alignment direction. Scale bar: $100 \, \mu m. \, c, \, d$ SHG and SHG-I analysis

of the polar ordering of the NJU001 material for Pathway I and Pathway II. The SHG images in the N and NF phases are at 80 °C and 57 °C, respectively; the rest of the SHG and SHG-I images are at 65 °C. The double-headed white arrows indicate the incident polarization. The red and blue arrows denote the polarization vectors in these regions. SHG: second-harmonic generation; SHG-I: SHG interferometry. Scale bar: $25\,\mu m$. Source data are provided as a Source Data file.

region also exhibits the apolar nematic order along the same orientation in adjacent stripes, supporting Unipolar model A. The invalidity of Unipolar model B is also directly visualized by the fluorescence confocal polarizing microscopy (FCPM), where uniform green textures with no visible domain wall are observed under the circular

polarization excitation (Supplementary Fig. S15a). These results correspond to the director oriented in the x-y plane⁴². Thus, we can rule out the possibility of models with out-of-plane orientational order components, like Unipolar model B, and dipoles in the Bloch domain wall.

The second one, Pathway II, of forming periodic bipolar stripes, a concept analog to bipolar voltages with both positive and negative voltages referenced to zero volts, is rather trivial when considering the formation of the anti-polar nematic phase (Fig. 2a-ii). The PLM and SHG results at different temperatures in Pathway II display similar patterns to those of Pathway I (Supplementary Fig. S16, Fig. 2d, and Supplementary Fig. S11b). However, SHG-I imaging, in this case, reveals alternating bright and dark variations between adjacent stripes, suggesting constructive and destructive interference, respectively. Namely, when the interference condition changes by a phase difference of π , the brightness of the stripes is reversed, indicating a nearly π phase shift in the polarization vectors between adjacent stripes, as denoted by the red and blue arrows. By employing similar structural analyses made for Pathway I, we find the transitional region between the stripes in Pathway II also shows the apolar nematic ordering along the orientation in adjacent stripes (Bipolar model; Fig. 2a-ii, Supplementary Figs S14c,d, and S15b). These observations exclude some inconsistent models, such as the Splay nematic model with disclinations (Fig. 2a-ii), Ising, Néel, and Bloch models (Supplementary Fig. S17, Supplementary Section 3).

To understand the mechanism of why domain walls accompanied by clear defects were not observed experimentally, we employ an extended Oseen-Frank free-energy functional³⁹ to conduct numerical simulations. Essentially, both the apolar and polar Landau energy terms^{39,43} are included to consider the stabilities of the apolar and polar orientational orders. The total free energy density in bulk reads:

$$\begin{split} & f_{\text{total}} = f_{\text{elast}} + f_{\text{L,A}} + f_{\text{L,P}} + f_{\text{grad}} + f_{\text{flexo}} + f_{\text{depol}} \\ &= \frac{K_{11}}{2} \left[\nabla \cdot \mathbf{n_0} S \right]^2 + \frac{K_{22}}{2} \left[\mathbf{n_0} S \cdot \left(\nabla \times \mathbf{n_0} S \right) \right]^2 + \frac{K_{33}}{2} \left[\mathbf{n_0} S \times \left(\nabla \times \mathbf{n_0} S \right) \right]^2 + \\ &\frac{1}{2} a S^2 + \frac{1}{2} b S^4 + \frac{A|\mathbf{P}|^2}{2} + \frac{B|\mathbf{P}|^4}{2} + \frac{h}{2} |\nabla \mathbf{P}|^2 - \gamma \mathbf{n_0} S \left(\nabla \cdot \mathbf{n_0} S \right) \cdot \mathbf{P} - \frac{1}{2} \mathbf{P} \cdot \mathbf{E_d} \end{split}$$

The first three terms are Frank elastic energies ($f_{\rm elast}$) describing the splay (K_{11}) , twist (K_{22}) , and bend (K_{33}) deformations. The nematic director **n** is defined by a product of the unit orientational vector \mathbf{n}_0 and the apolar orientational order parameter S, $\mathbf{n} = \mathbf{n_0} S$. The fourth and fifth terms are apolar Landau energies $(f_{L,A})$. The sixth and seventh terms are polar Landau energies $(f_{L,P})$. The polarization is defined as $\mathbf{P} \equiv P_0 S_{\rm P} \mathbf{n_0}$ since dipoles are along the director in polar nematics⁴³. P_0 is the maximum value that the polarization can take. The Landau energies determine equilibrium values of the apolar and polar orientational order parameters, i.e., S and S_p . The eighth to tenth terms are polar interaction energies, corresponding to the polarization gradient $(f_{\rm grad})$, flexoelectric $(f_{\rm flexo})$ and electrostatic $(f_{\rm depol})$ energy terms, respectively. γ is the flexoelectric coefficient. Importantly, S and S_P can be either coupled (i.e., P-n coupled case) or decoupled (i.e., P-n decoupled case), depending on the primary driving force for forming a nematic phase. If the anisotropic dipole-dipole interaction is the only trigger for getting a nematic phase (i.e., the shape anisotropy is not high enough for forming the apolar nematic phase), the phase is then polar, and S should be identical to S_P . On the other hand, S_P would be decoupled from S if the polar order is induced by high enough S^{43} . In this case, a finite S_P arises only when S exceeds a threshold. To account for the surface anchoring imposed by photoalignment of the nematic director, we only consider the apolar anchoring potentials:

$$f_{\text{surf}} = \frac{1}{2} W_{\text{A}} \left[1 - (\mathbf{n} \cdot \mathbf{a})^2 \right]$$
 (2)

where W_A and ${\bf a}$ are the anchoring strength and anchoring axis.

Based on the free-energy functionals, we search for how the coupling between the orientational order and polar interactions dictates polar textures. Our results find that flexoelectricity triggers the production of the splayed polar fields. The competition between the energy costs of two Landau and flexoelectric energies determines how

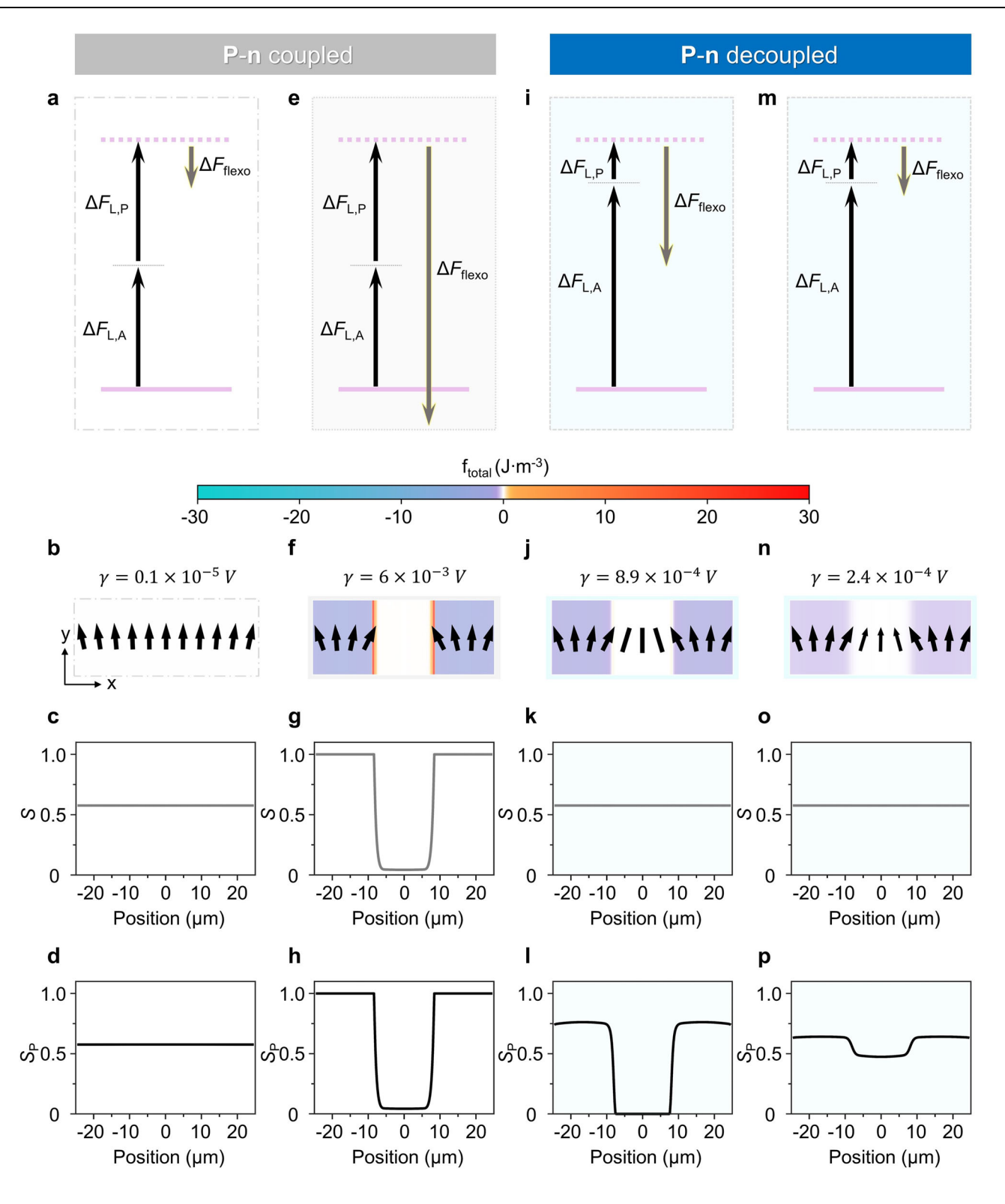
local polar orders in the Nx phase would be revised and what types of domain walls, e.g., singular or nonsingular, would be generated (Fig. 3). Figure 3 demonstrates four representative unipolar fields, which evolve from emerging two syn-parallel aligned polar domains from the N phase as seen in experiments (Fig. 2c), simulated under **P-n** coupled (Fig. 3a. e) and decoupled (Fig. 3i. m) conditions.

When S and S_P are coupled, it means the polar order primarily controls the appearance of the polar nematic phase. In Fig. 3a, we consider a weak flexoelectric interaction, i.e., small γ , in a very stable polar nematic phase. Locally, flexoelectricity tends to generate a spontaneous positive splay that lowers its free energy by $-\gamma \mathbf{n_0} S(\nabla \cdot \mathbf{n_0} S)$, and dislikes the negative one⁴⁰. The polarization gradient and electrostatic effects are assumed to be less important in the Nx phase, where the polar order is small. Since the stable orientational orders are guaranteed by large apolar and polar Landau energy terms, flexoelectricity just serves as a weak disturber for the polar field. Namely, the order parameters, $S = S_P$, are nearly unchanged from their equilibrium values while some local positive splay is induced (Fig. 3b-d). Flexoelectricity starts to be able to compete with the stability of the orientational orders (large γ as in Fig. 3e) when the variation of the volume integral of f_{flexo} (ΔF_{flexo}) is comparable or larger than that of $f_{L,A} + f_{L,P}$ ($\Delta F_{L,A} + \Delta F_{L,P}$) upon an orientational change. Therein, nontrivial local polar fields emerge. In the two synparallel aligned polar domains, a positive splay is stabilized. In between them, a negative splay orientational region is automatically produced by the nematic elastic interaction. However, the negative splay is unstable because flexoelectricity should pay a large energy penalty by $\gamma \mathbf{n_0} S(\nabla \cdot \mathbf{n_0} S)$. Since the Landau terms consume less energy, the negative splay is destroyed by melting all the orientational orders, i.e., local $S = S_P \sim 0$ (Fig. 3f-h). This leads to a sharp reduction of S and S_P between the polar and isotropic regions, resulting in a singular domain wall that corresponds to a defect line.

Next, we turn to the situation with S and S_P decoupled. This scenario is closer to what happens in our system because the Nx phase appears after the N phase has already developed. Namely, SP is the secondary order parameter induced by S. Therefore, it is reasonable that the apolar orientational order is much more stable than the polar orientational order. In the free-energy landscape, the magnitude of the apolar Landau energy must be much larger than the polar counterpart (Fig. 3i, m). For simplicity, we completely decouple S and S_P by fixing S = 0.58, taking care of infinitely stable apolar orientational order, while S_P is variable in our numerical simulations (Fig. 3k, o). Now, the flexoelectric interaction merely competes against the polar Landau energy. The balance between ΔF_{flexo} and $\Delta F_{\text{L,P}}$ again plays an important role to determine microscopic topology. When $\Delta F_{\text{flexo}} \gg \Delta F_{\text{L.P}}$ (e.g., $\gamma = 8.9 \times 10^{-4}$ V), the negative splay region separating the neighboring polar domains ends with an unpolarized state to save the flexoelectric energy (Fig. 3j). Importantly, the apolar orientational order is retained, i.e., S > 0 and $S_P = 0$. A defect line appears because the spatial variation of S_P , i.e., ∇S_P , is discontinuous from the polar to apolar regions (Fig. 3l and Supplementary Fig. S18). With decreasing the influence of the flexoelectricity, the discontinuity of $\nabla S_{\rm p}$ decreases and jumps to a quasi-continuous one when ν is below 3.4×10^{-4} V (Fig. 3n and Supplementary Fig. S18). Figure 3p illustrates a simulated polar field with its order parameters as a function of the coordinate. Unlike Fig. 3l, as a surprise, $S_{\rm P}$ remains finite, and there is a nonsingular domain wall. The nonsingularity across the middle and twosided polar regions, where the magnitude of the polarization differs, indicates the absence of visible defect structures. This is consistent with our experimental observation of alternative splayed regions with modulated polarity, evidenced by bright-dark-bright stripes in SHG microscopies (Fig. 2c and Supplementary Fig. S11a).

Programmable domain engineering

We achieve numerous large-scale polar patterns to demonstrate the feasibility of defect-free domain engineering in the Nx mesophase. We



implement two types of patterning for the NJU001 material: (1) continuous spatially-variant polar patterns; (2) binary polar patterns. In the first case, we investigate a periodic alternating splay and bend configuration (Fig. 4a), which is mathematically expressed as: $\hat{\bf n}(x,y,z)=(\cos\frac{\pi x}{A},\sin\frac{\pi x}{A},0)$. Λ represents the pattern period. We capture PLM images in N, Nx, and NF phases under crossed polarizers (Fig. 4a–c). Both the N and Nx phases display high-quality, defect-free textures with periodic extinctions where LC directors are either parallel or perpendicular to the polarizers. This suggests a uniform alignment of LC directors across the cell thickness direction, i.e., no

twists. As the system enters the NF phase, the polar field is significantly distorted. The texture no longer exhibits extinction due to the presence of twists⁴⁴. The difference in the regularity of the patterns can be quantified by comparing the cross-sectional profiles of the transmitted intensity. In the second case, we design three binary images as templates: a 12-fold symmetric quasicrystal, the letters "NJU", and a logo of Nanjing University (Fig. 4d-f). Then, we transfer them to the corresponding polar patterns. We observe defect-free polar patterns that emit sharp-contrast SHG patterns, well consistent with our template images. These results highlight the high-quality domain engineering

Fig. 3 | **Flexoelectricity-driven formation of polar textures. a**-**d** Polar order dominating the appearance of the polar nematic phase under the condition of coupled S and S_P with a weak flexoelectric interaction. **a** Schematic of energy competition among the Landau energies ($\Delta F_{\rm L,A}$ and $\Delta F_{\rm L,P}$ for apolar and polar Landau energy penalties upon an orientational change) and flexoelectricity ($\Delta F_{\rm flex}$ for energy penalty of flexoelectric upon an orientational change). **b** Total free energy density distribution $f_{\rm total}$. The black arrows denote the polar orientation ordering. **c** Apolar orientational order parameters as a function of the coordinate. **d** Polar orientational order parameters as a function of the coordinate. **e**-**h** Polar order dominating the appearance of the polar nematic phase under the condition of coupled S and S_P with a strong flexoelectric interaction. **e** Schematic of energy competition among the Landau energies and flexoelectricity. **f** Total free energy density distribution $f_{\rm total}$. **g** Apolar orientational order parameters as a function of the coordinate. **h** Polar orientational order parameters as a function of the coordinate. **i**-**l** Flexoelectric interaction merely competing against the polar Landau

energy under the condition of decoupled S and S_P , $\Delta F_{flexo}\gg \Delta F_{L,P}$. **i** Schematic of energy competition between the polar Landau energy and flexoelectricity. **j** Total free energy density distribution f_{total} . The black bars denote the apolar orientation ordering. **k** Apolar orientational order parameters as a function of the coordinate. **l** Polar orientational order parameters as a function of the coordinate. **m**–**p** Flexoelectric interaction merely competing against the polar Landau energy under the condition of decoupled S and S_P , $\Delta F_{flexo} > \Delta F_{L,P}$. **m** Schematic of energy competition between the polar Landau energy and flexoelectricity. **n** Total free energy density distribution f_{total} . The downsized black arrows denote the decreasing magnitude of polarization. **o** Apolar orientational order parameters as a function of the coordinate. **p** Polar orientational order parameters as a function of the coordinate. Other parameters used for numerical calculations can be found in Methods. Source data are provided as a Source Data file.

capability in the Nx mesophase and its usefulness in tailoring functional nonlinear photonic devices. As a photorealistic application in both the linear and nonlinear optical regimes, we showcase a reproduction of the famous artwork, "Girl with a Pearl Earring" in Fig. 4g, which features grayscale variations comprising both continuous gradients and discontinuous steps. By encoding the brightness of the artwork (from 0 to 255) into the spatially-variant polar field (top panels in Fig. 4h, i), we successfully generate high-resolution PLM and SHG arts (Fig. 4h, i).

Nonlinear vectorial liquid-crystal optics

When an input polarized FW excites a nonlinear medium belonging to the point group $C_{\infty V}$ (e.g., polar LCs composed of oriented dipoles), a nonlinear polarization field arises as (Supplementary Section 4):

$$\mathbf{P}_{\alpha}^{2\omega} = 2A_{0}^{2}\varepsilon_{0}d_{33}\cos^{2}(\phi - \alpha)\hat{\mathbf{e}}_{\alpha}$$

$$= 2A_{0}^{2}\varepsilon_{0}d_{33}\cos(\phi - \alpha)\begin{pmatrix} \cos^{2}\alpha & \cos\alpha\sin\alpha\\ \cos\alpha\sin\alpha & \sin^{2}\alpha \end{pmatrix}\begin{pmatrix} \cos\phi\\ \sin\phi \end{pmatrix}$$
(3)

 A_0 is the amplitude of FW, ε_0 the vacuum permittivity, d_{33} the nonlinear coefficient, ω the angular frequency, ϕ the polarization angle relative to the x-axis, α the azimuthal angle of the dipole, and $\hat{\mathbf{e}}_{\alpha}$ the unit vector along the α direction, ($\cos \alpha \atop \sin \alpha$). The intensity is proportional to the quartic amplitude of the electric field of FW,

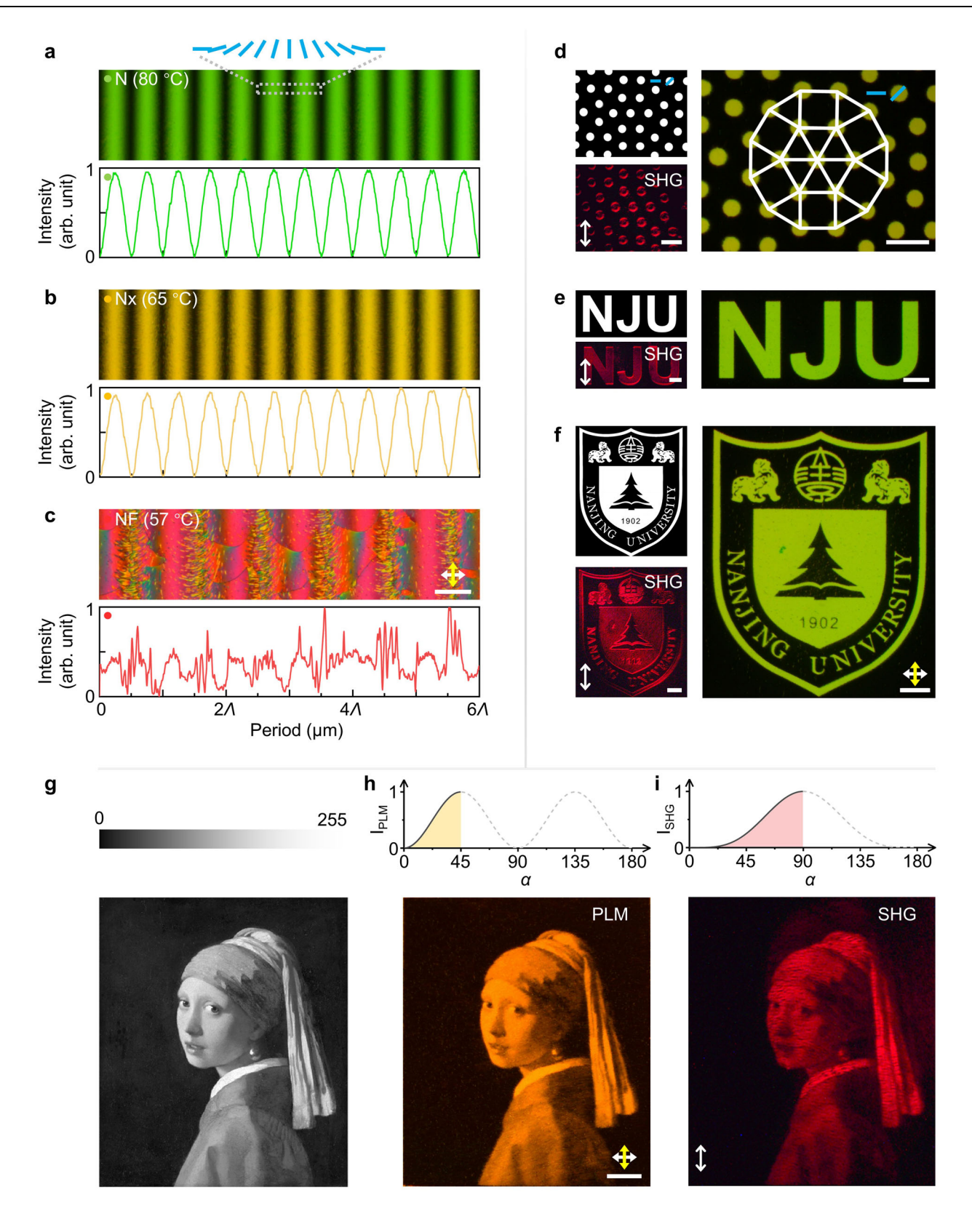
$$I^{2\omega}(\alpha) \propto A_0^4 \cos^4(\phi - \alpha)$$
 (4)

These relationships bear a striking resemblance to the light propagation through a linear polarizer and the well-established Malus's law (Supplementary Section 5). The oriented polar LCs is characterized by a Jones matrix formalism: $\cos(\phi-\alpha)(\frac{\cos^2\alpha}{\cos\alpha\sin\alpha}\frac{\cos\alpha\sin\alpha}{\sin^2\alpha})$, endowing the system with two distinct capabilities: (1) the nonlinear optical response governed by the material's nonlinearity; (2) the selective excitation of instantaneous electric field vector, which follows the polar LC's orientation α across the full angular range $[0, 2\pi]$ (Supplementary Fig. S19).

As a proof-of-concept demonstration, we demonstrate the capability of generating both linear and nonlinear perfect vector beams (PVBs) using a single-layer patterned polar LC device (Fig. 5a). As a new type of vector beam⁴⁶ with cylindrical symmetry in polarization, PVB has sparked considerable interest because its radius and intensity profile are independent of the polarization topological charge *l*, demonstrating superior capabilities in optical manipulation, microscopy imaging, and laser micromachining. Although PVBs have been widely studied in the framework of linear optics^{47,48}, the direct

generation of SH PVBs from a single nonlinear optical element has not been realized due to previous challenges in manipulating in-plane polar ordering. Here, we design the orientation distribution α of polar LCs based on Eqs. (3) and (4), taking into account the near-field polarization, phase, and intensity distributions. Supplementary Fig. S20a depicts the designed orientation distribution of polar LCs, $\alpha = \frac{1}{2}l\varphi + \frac{1}{2}\arg\left[2\sum_{n=1}^{\infty}a_n\sin\left(2\pi\frac{n}{T}r\right)\right], r \ge 0.$ a_n represents the Fourier series coefficients, $T = 100 \, \mu \text{m}$ is the period of concentric rings, r and φ denote the radial distance and azimuthal angle in the polar coordinate, and *l* is the polarization topological charge. In this case, the simulated near-field instantaneous electric field vector, when Fouriertransformed to the far field, enables an intensity profile and polarization distribution that meet the criteria of a nonlinear perfect vector beam. Accordingly, we show the surface anchoring pattern for both substrates of the device in Fig. 5a. The alignment direction continuously changes in the azimuthal angle, and the orientations in adjacent rings maintain a consistent perpendicular relationship in the radial direction. By employing photoalignment technology in conjunction with a self-developed digital micromirror device-based microlithography system ("Methods")34,49, we achieved high-quality in-plane polar LC domain engineering, accomplished through the effective utilization of surface anchoring energy to dictate the LC orientation. The resulting polar LC superstructure is characterized under a crossed-PLM, which highlights the unique hierarchical and topological features of our device, incorporating both continuous and discontinuous variations of dipole orientations. The visible Maltese cross and the periodic circular domain walls shown in Fig. 5b and Supplementary Fig. S20b indicate that the LC director orientations are faithfully imprinted according to our design. A schematic of a crosssection of the LC cell is provided in Supplementary Fig. S21. The polar ordering is further confirmed by SHG-I imaging (Supplementary Fig. S22), with the local polar orientation distribution at the center shown in Fig. 5c.

Upon a linearly polarized FW excitation (ϕ = 90°), a PVB in the realm of linear optics (polarization topological charge |l| = 2) is generated due to the imprinted linear geometric phase⁵⁰ (Fig. 5d and Supplementary Fig. S23; Supplementary Section 6). Simultaneously, an SH vector beam with a ring-shaped intensity profile is also obtained (the first panel in Fig. 5e). The vector nature is further characterized by using an adjustable analyzer behind the device (the second and third panels in Fig. 5e). Extinction occurs when the polarization is perpendicular to the analyzer. Therefore, by examining the locations of extinction, the nonlinear PVB with a specific space-variant polarization distribution is confirmed, as shown in the upper right corner of the first panel of Fig. 5e. The polarization topological charge is determined to be l=2. These results align well with the expected intensities and polarization distributions (Supplementary Section 6 and Supplementary Fig. S24). More importantly, the perfect virtue of vector beams in



both linear and nonlinear optical frameworks is verified, characterized by the invariant radius and intensity profiles under changing polarization topological charges (|l| = 1, 2, ..., 6; Fig. 5f, g, and Supplementary Fig. S25) of the vector beams, which is vital for applications in high-capacity information processing technology and so on²⁵.

Furthermore, by leveraging the dynamic tunability of LCs, we demonstrate active and reversible switching of SH-PVBs under an ultra-

low electric field. When applying a triangular electric field (peak-to-peak voltage $V_{\rm pp}$ = 0.12 V/µm, frequency f = 0.5 Hz) across the device, the topological polar LC superstructure exhibits periodic switching behavior (Fig. 5h, i). This results in a dynamically tunable nonlinear vector optical field with periodic on-off features (Fig. 5j). More details are provided in Supplementary Section 7.

Fig. 4 | **Programmable domain engineering in the Nx phase.** \mathbf{a} - \mathbf{c} PLM textures and intensity profiles of the continuous spatially-variant polar pattern in N, Nx, and NF phases. The blue bars in (\mathbf{a}) represent the alignment configuration. The red arrows in (\mathbf{b}) denote the dipole distribution. The white and yellow arrows represent the crossed polarizers. A is 171 μ m. N: nematic phase; NF: ferroelectric nematic phase. \mathbf{d} - \mathbf{f} Preset alignment patterns, PLM textures, and SHG images of the binary polar patterns, including a 12-fold symmetric quasicrystal, the letters "NJU", and the logo of Nanjing University in the Nx phase. The alignment directions are denoted by blue bars. The double-headed white arrows indicate the incident polarization of FW. The school badge pattern of Nanjing University is reproduced with permission of Nanjing University. SHG: second-harmonic generation. \mathbf{g} A reproduction of "Girl

with a Pearl Earring" by Johannes Vermeer (c. 1665) formed by converting it to a grayscale image. The original artwork is in the public domain 4 . The grayscale values from 0 to 255 are proportionally mapped to the distribution of α . **h,i** Reproduction arts of "Girl with a Pearl Earring" by Johannes Vermeer (c. 1665) 4 5 formed by patterned polar LCs. One is imaged under PLM, and the other is the SHG image exited by a femtosecond laser. The original artwork "Girl with a Pearl Earring" is in the public domain. The alignment distributions are calculated according to the equations of $\alpha \propto \frac{1}{2} \arcsin(\sqrt{I_{\rm PLM}})$ and $\alpha \propto \arcsin(\sqrt[4]{I_{\rm SHG}})$, where α is the azimuthal angle of the local dipole in the ranges of (0°, 45°) and (0°, 90°), respectively. Scale bars: 100 µm. PLM: polarized light microscopy. Source data are provided as a Source Data file.

Discussion

Systems that exhibit phase competition, order parameter coexistence, and emergent order parameter topologies constitute a crucial part of modern condensed-matter physics⁵¹. In this work, we establish a key link between paraelectric (apolar) and ferroelectric (polar) states, based on a distinct liquid of ferroelectrics with nematicity, which acts as an intermediate state between the recently identified ferroelectric nematic and traditional apolar nematic phases. A new structural model is established with our extended Oseen-Frank free-energy functional, which elucidates the formation of the unique unipolar and bipolar orderings in this mesophase. Importantly, the discovered polar orders make a sharp contrast to the existing NF order in the structure, and demonstrate a better potential in domain engineering for developing nonlinear optical elements. For the former, this study reveals a novel energy competition scenario among the Landau energies ($\Delta F_{L,A}$ and $\Delta F_{1 P}$ for apolar and polar Landau energy penalties) and flexoelectricity (ΔF_{flex}) with decoupled S and S_P . It means that carefully adjusting multiple energy landscapes with either coupling or decoupling polar and LC nematic orders would trigger a broad range of unknown polar orders. For the latter, the Nx phase exhibits an exceptional capability of in-plane polar domain engineering. Though preceding works have shown that NF order can be employed to generate pure splay orientational patterns with good quality^{34,36,52}, complex hierarchical architectures with customizable (e.g., with more complicated deformations with bending), precise, and defect-free polar ordering on a large scale is difficult (see defect-mediated NF structure in Fig. 5b-iv, Supplementary Figs. S16, and S20). The Nx order has shown the capability to overcome these drawbacks, enabling hierarchical topological superstructures that surpass the azimuthal complexity of polar orientational field designs like prior q-plate³⁴ and periodic splay patterns^{36,52}, yielding high-performance nonlinear perfect vector beams - a capability neither previously conceptualized nor realized in the NF phase. This may provide an exciting platform for developing new ferroelectric materials with tailored properties and for exploring emergent phenomena in condensed-matter physics and nonlinear photonics.

As photonics technology advances from scalar to vectorial regimes^{30,53-56}, the construction of nonlinear vectorial light fields has become increasingly essential for applications including superresolution imaging⁵⁷, high-capacity optical communications⁵³, and high-precision laser micromachining⁵⁸. Note that creating such vectorial nonlinear modes would require several passes through a spatial light modulator (lossy) or mixing beams with interferometry (difficult to align), demanding complex optical systems with cascaded linear and nonlinear light field manipulation. Here, the generation of SH PVBs is achieved directly from a single, miniaturized polar LC device under a scalar Gaussian FW incidence, thanks to the flexible tailoring of tunable polar topologies. This is a feat that has not yet been accomplished with other ferroelectric materials. Such intriguing light-matter interaction could lead to the next generation of portable, scalable, and reconfigurable photonic technologies with wide-ranging applications, e.g., alloptical communications, quantum computing, soft intelligent robotics, and the biomedical industry.

Methods

Materials

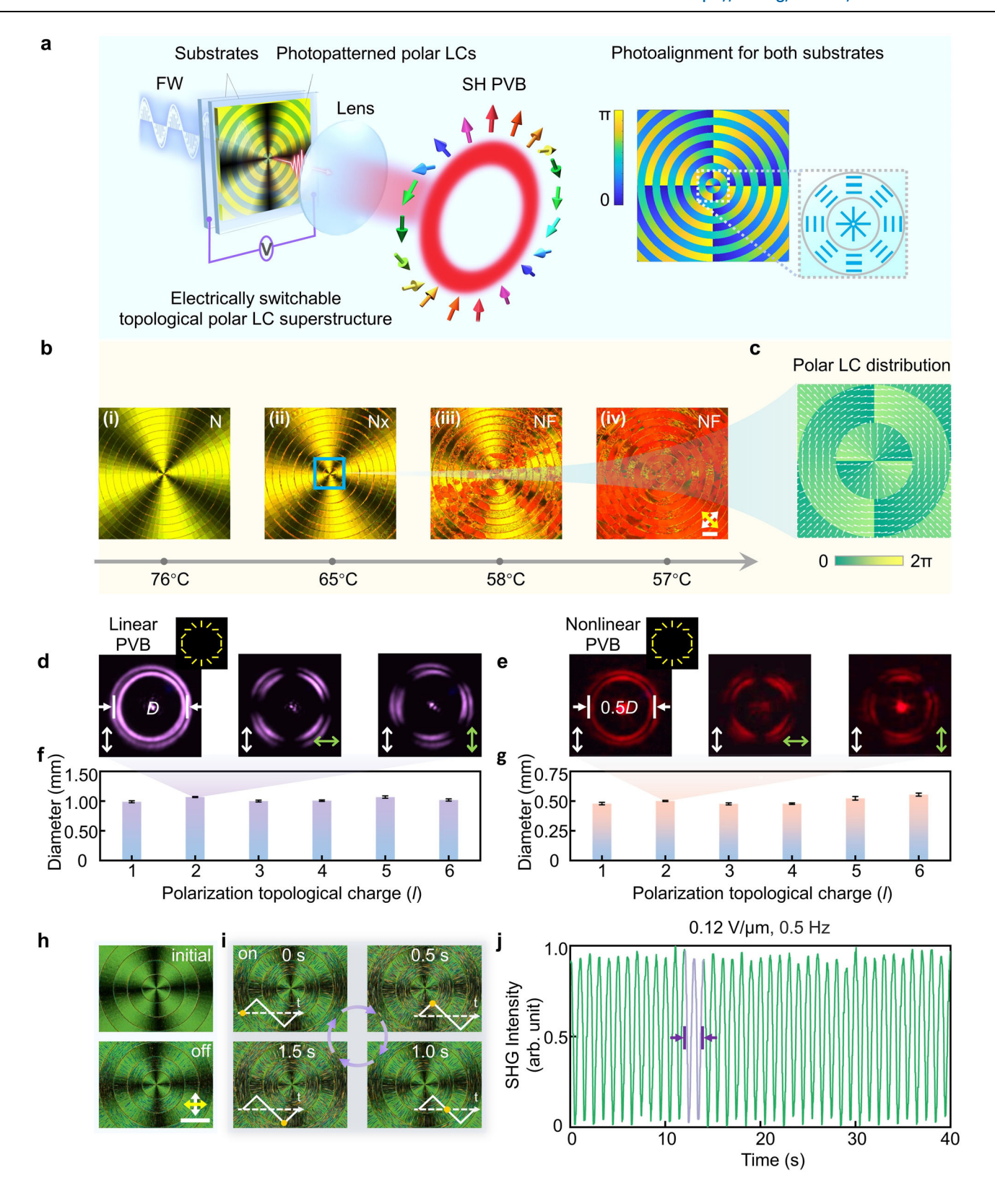
The agent SD1 (provided by Nanjing Ningcui Optical Technology Co., Ltd., China) was used for the photoalignment. SD1 molecules are susceptible to the linear polarization of exposure light. These molecules undergo isomerization upon absorbing ultraviolet photons and eventually align perpendicularly to the local polarization due to their dichroic absorption properties^{59,60}. Notably, SD1 is rewritable, with only the final photo reorientation being recorded. Once the LC material is infiltrated, the SD1 layer guides the LC molecules through intermolecular interactions. The synthesis flow of the polar nematic NJU001 material is provided in Supplementary Section 1.

Fabrications

Indium-Tin-Oxide-coated glass substrates were first ultrasonically cleaned, then UV ozone cleaned. Then, the alignment agent SD1 was dissolved in dimethylformamide at 0.35 wt%, spin-coated onto the substrates, and annealed at 100 °C for 10 min. Two glass substrates were separated by spacers, which determine the cell gap, and sealed with epoxy glue to form an LC cell. We used untreated cells for the transient current (P-E loops) measurements (results in Fig. 1f, g and Supplementary Fig. S8; cell thickness: 10 µm), PLM observations of the NIU001 material (schlieren texture in Supplementary Fig. S7), and PolScope (results in Supplementary Fig. S9; cell thickness: 8.5 µm). If not specifically denoted, the tests in our work employed LC cells of a cell gap of 4 µm that were photoaligned. To achieve photo-aligned LC cells, empty cells were placed at the image plane of the digital micromirror device-based microlithography system to record the target patterns via a multistep, partly overlapping exposure process with synchronous polarization control. The SD1 alignment layers on both substrates were simultaneously photoaligned. We summarize the alignment pattern in Supplementary Fig. S26. The NJU001 material was then infiltrated into the LC cells at 135 °C and slowly cooled to the target temperatures.

Characterizations

The ordering in the Nx phase was characterized by employing PLM, SHG, SHG-I, and FCPM. The PLM textures of NJU001 material were captured using a PLM (DM2700P, Leica), which allows for detailed observations of the texture and optical anisotropic properties. The optical path for SHG and SHG-I measurements is shown in Supplementary Fig. S12. A Q-switched pulsed laser (MPL-277 III-1064; central wavelength: 1064 nm; pulse duration: 5 ns; repetition rate: 100 Hz) was used as the FW. The SH light was detected in the transmission or reflection (backward) geometry by a photomultiplier tube (DH-PMT-D100V, Daheng Optics) or a scientific complementary metal-oxidesemiconductor (CMOS) camera (Zyla-4.2P-USB3, Andor). FCPM observations were carried out using an inverted microscope with a halogen illuminator (Zeiss HAL 100) and objective lenses of ×20 (NA = 0.80) and \times 40 (NA = 0.95) magnifications. Fluorescent dye N,N'-Bis(2,5-di-tert-butylphenyl)-3,4,9,10-perylenedicarboximide Sigma-Aldrich) was used to label the LC orientations, with a concentration of 0.05 wt% mixed into the NJU001. These dyes will align



parallel to the LC molecules. The fluorescence intensity excited with circularly polarized light was sensitive to the tilt angle of the LC directors. Thus, circularly polarized light at 488 nm was employed to excite BTBP, and the presence of out-of-plane LC orientation can be deduced. The transient current measurements of the NJU001 material were performed using a ferroelectric property analyzer (TOYO FCE10-S, Japan) in conjunction with a Sawyer-Tower circuit.

Numerical modeling

We utilized the finite element method to numerically calculate the spatial distribution of polar and orientational orders and the relevant free-energy density mappings based on Eq. (1). The relaxation process was conducted using the Euler-Lagrange method in MATLAB. The viscosity and the time interval for the simulation were set to $1 \times 10^{-7} \, \text{Pa-s}$ and 1 ns, respectively, with typically 10^{5} iteration steps to

Fig. 5 | **Miniaturized tunable nonlinear vectorial photonic devices.** a Schematic of LC-based nonlinear vectorial optics. This photonic functionality is enabled by the flexible tailoring of the polar ordering in the miniaturized PVB generation device. The photoalignment patterns for the two substrates of the LC device are the same, as shown in the right panel. LCs: liquid crystals; FW: fundamental wave; PVB: perfect vector beam. **b** Texture evolution of the toroidal topological polar LC superstructure during cooling. N: nematic phase; NF: ferroelectric nematic phase. The white and yellow arrows denote the crossed polarizers. Scale bar: 100 μm. **c** Resulting polar ordering of the topological LC superstructure. **d, e** Linear and nonlinear PVBs generated from the LC device, along with their analyzed intensity profiles. The diameter of the nonlinear PVB is approximately half that of the linear PVB due to the frequency conversion. The white and green double-headed arrows

indicate the incident polarization and the direction of the analyzer, respectively. The polarization distributions of the PVBs are provided in the upper right corners of the first panels of (**d**) and (**e**). D: diameter. **f**,**g** Dependences of the ring diameter on the polarization topological charge (|l|=1-6). Error bars represent mean \pm standard deviation. **h** Textures before and after the application of the electric field. **i** Typical textures captured in one cycle of an applied triangular wave. The voltage is \pm 0.12 V/µm, and the frequency is 0.5 Hz. **j** Periodic switching of the intensity of the SH PVB by electrically tuning the dipoles in the superstructure from the transverse direction to the longitudinal direction. The purple part highlights the SHG intensity change within one cycle of an applied triangular wave. SHG: second-harmonic generation. Source data are provided as a Source Data file.

ensure the system reaches equilibrium. We set a one-dimensional mesh network with a dimension of 50 μ m \times 0.2 μ m and a mesh spacing of 200 nm. The parameters for the numerical calculations were set as follows: the elastic constants of LCs were defined using the oneconstant approximation, i.e., $K_{11} = K_{22} = K_{33} = 1$ pN. The maximum value of the polarization P_0 is 6.0 μ C·cm⁻², which is a typical value in polar LCs³³. The phenomenological coefficients in the apolar and polar Landau energies were specified as a = -2 J·m⁻², b = 3 J·m⁻², A = -550 $J \cdot m \cdot C^{-2}$ and $B = 2.3 \times 10^5 J \cdot m^5 \cdot C^{-4}$. The equilibrium apolar and polar orientational order can be found from Landau terms, giving S = 0.58and $S_P = 0.58$, respectively. The polarization gradient coefficient was set as $h = 1 \times 10^{-10} \,\text{J} \cdot \text{m}^3 \cdot \text{C}^{-2}$. The surface anchoring strength was chosen as $W_A = 6 \times 10^{-7} \text{ J} \cdot \text{m}^{-2}$. y is a flexoelectric coefficient relating to the splay deformation. For the **P-n** coupled condition, we assume $S = S_P$ for simplicity because the orientational order is directly induced by the polar order (Fig. 3a, e). For the **P-n** decoupled condition, S is fixed at 0.58 and S_p is a variable, where the apolar nematic orientational order is assumed to be stable (Fig. 3i, m).

Data availability

The data generated in this study have been deposited in the Figshare database under the accession code https://doi.org/10.6084/m9. figshare.30023326. Source data are provided in this paper.

Code availability

The calculations can be done following the instructions in Methods and Supplementary Information. The code related to this study is available upon request.

References

- Uehara, M., Mori, S., Chen, C. H. & Cheong, S. W. Percolative phase separation underlies colossal magnetoresistance in mixed-valent manganites. *Nature* 399, 560–563 (1999).
- Jin, S. et al. Thousandfold change in resistivity in magnetoresistive La-Ca-Mn-O films. Science 264, 413–415 (1994).
- 3. Qiu, Z. et al. Spin colossal magnetoresistance in an antiferromagnetic insulator. *Nat. Mater.* **17**, 577–580 (2018).
- Tang, J. et al. Magnetic skyrmion bundles and their current-driven dynamics. Nat. Nanotechnol. 16, 1086–1091 (2021).
- Chen, S. et al. Recent progress on topological structures in ferroic thin films and heterostructures. Adv. Mater. 33, 2000857 (2020).
- Bogdanov, A. N. & Panagopoulos, C. Physical foundations and basic properties of magnetic skyrmions. *Nat. Rev. Phys.* 2, 492–498 (2020).
- Yu, X. Z. et al. Transformation between meron and skyrmion topological spin textures in a chiral magnet. Nature 564, 95–98 (2018).
- 8. Boyd, R. W. Nonlinear Optics. 3rd edn, (Academic Press, 2008).
- 9. Zhu, S. -n, Zhu, Y. -y & Ming, N. -b Quasi-phase-matched third-harmonic generation in a quasi-periodic optical superlattice. *Science* **278**, 843–846 (1997).
- 10. Yang, W., Kazansky, P. G. & Svirko, Y. P. Non-reciprocal ultrafast laser writing. *Nat. Photonics* **2**, 99–104 (2008).

- 11. Wu, S. T. & Yang, D. K. Fundamentals of Liquid Crystal Devices. (John Wiley & Sons, 2014).
- Ma, L. L. et al. Self-assembled liquid crystal architectures for soft matter photonics. *Light. Sci. Appl.* 11, 270 (2022).
- 13. Zhang, P., Wang, G. & Yu, H. Ultraviolet-visible-near-infrared light-responsive soft materials: Fabrication, photomechanical deformation and applications. *Responsive Mater.* **2**, e20240016 (2024).
- Zhang, Y., Zheng, Z. G. & Li, Q. Multiple degrees-of-freedom programmable soft-matter-photonics: Configuration, manipulation, and advanced applications. Responsive Mater. 2, e20230029 (2024).
- Zheng, R. et al. Stimuli-responsive active materials for dynamic control of light field. Responsive Mater. 1, e20230017 (2023).
- Ware, T. H., McConney, M. E., Wie, J. J., Tondiglia, V. P. & White, T. J. Voxelated liquid crystal elastomers. Science 347, 982–984 (2015).
- Wang, X., Miller, D. S., Bukusoglu, E., de Pablo, J. J. & Abbott, N. L. Topological defects in liquid crystals as templates for molecular self-assembly. *Nat. Mater.* 15, 106–112 (2016).
- Koizumi, R. et al. Topological transformations of a nematic drop. Sci. Adv. 9, eadf3385 (2023).
- Wu, J.-S. & Smalyukh, I. I. Hopfions, heliknotons, skyrmions, torons and both abelian and nonabelian vortices in chiral liquid crystals. *Liq. Cryst. Rev.* 10, 34–68 (2022).
- Ma, L.-L. et al. Programmable self-propelling actuators enabled by a dynamic helical medium. Sci. Adv. 7, eabh3505 (2021).
- Lin, X., Shi, D., Yi, G. & Yu, D. Structural color-based physical unclonable function. Responsive Mater. 2, e20230031 (2024).
- 22. Ma, L.-L., Wei, Y., Wang, N., Chen, W. & Lu, Y.-Q. Soft matter photonics: interplay of soft matter and light. ACS Nano 19, 11501 (2025).
- Chen, P., Wei, B. Y., Hu, W. & Lu, Y. Q. Liquid-crystal-mediated geometric phase: from transmissive to broadband reflective planar optics. Adv. Mater. 31, 1903665 (2019).
- Maurer, C., Jesacher, A., Fürhapter, S., Bernet, S. & Ritsch-Marte, M. Tailoring of arbitrary optical vector beams. N. J. Phys. 9, 78–78 (2007).
- 25. Li, P. et al. Generation of perfect vectorial vortex beams. Opt. Lett. 41, 2205 (2016).
- Wei, B.-Y. et al. Vortex Airy beams directly generated via liquid crystal q-Airy-plates. Appl. Phys. Lett. 112, 121101 (2018).
- 27. Mandal, A., Maji, S. & Brundavanam, M. M. Common-path generation of stable cylindrical perfect vector vortex beams of arbitrary order. *Opt. Commun.* **469**, 125807 (2020).
- 28. Bashkansky, M., Park, D. & Fatemi, F. K. Azimuthally and radially polarized light with a nematic SLM. Opt. Express 18, 212 (2020).
- Papic, M. et al. Topological liquid crystal superstructures as structured light lasers. Proc. Natl. Acad. Sci. USA 118, 2110839118 (2021).
- Liu, H., Li, H., Zheng, Y. & Chen, X. Nonlinear frequency conversion and manipulation of vector beams. Opt. Lett. 43, 5981 (2018).
- Mandle, R. J., Cowling, S. J. & Goodby, J. W. A nematic to nematic transformation exhibited by a rod-like liquid crystal. *Phys. Chem. Chem. Phys.* 19, 11429–11435 (2017).

- Nishikawa, H. et al. A fluid liquid-crystal material with highly polar order. Adv. Mater. 29, 1702354 (2017).
- Chen, X. et al. First-principles experimental demonstration of ferroelectricity in a thermotropic nematic liquid crystal: Polar domains and striking electro-optics. *Proc. Natl. Acad. Sci. USA* 117, 14021–14031 (2020).
- Pan, J.-T. et al. Nonlinear geometric phase coded ferroelectric nematic fluids for nonlinear soft-matter photonics. *Nat. Commun.* 15, 8732 (2024).
- Yang, J. D., Zou, Y., Li, J. X., Huang, M. J. & Aya, S. Flexoelectricitydriven toroidal polar topology in liquid-matter helielectrics. *Nat. Phys.* 20, 991 (2024).
- Sebastián, N. et al. Polarization patterning in ferroelectric nematic liquids via flexoelectric coupling. Nat. Commun. 14, 3029 (2023).
- 37. Medle Rupnik, P. et al. Antiferroelectric order in nematic liquids: flexoelectricity versus electrostatics. Adv. Sci. 12, 2414818 (2025).
- 38. Caimi, F. et al. Surface alignment of ferroelectric nematic liquid crystals. Soft Matter 17, 8130–8139 (2021).
- Zou, Y. & Aya, S. Extended free-energy functionals for achiral and chiral ferroelectric nematic liquid crystals: theory and simulation. *Phys. Chem. Chem. Phys.* 26, 15637–15647 (2024).
- 40. Mertelj, A. et al. Splay nematic phase. Phys. Rev. X 8, 041025 (2018).
- 41. Sebastian, N. et al. Ferroelectric-ferroelastic phase transition in a nematic liquid crystal. *Phys. Rev. Lett.* **124**, 037801 (2020).
- Smalyukh, I. I., Shiyanovskii, S. V. & Lavrentovich, O. D. Threedimensional imaging of orientational order by fluorescence confocal polarizing microscopy. *Chem. Phys. Lett.* 336, 88–96 (2001).
- Szydlowska, J. et al. Ferroelectric nematic-isotropic liquid critical end point. Phys. Rev. Lett. 130, 216802 (2023).
- 44. Kumari, P., Basnet, B., Lavrentovich, M. O. & Lavrentovich, O. D. Chiral ground states of ferroelectric liquid crystals. *Science* **383**, 1364–1368 (2024).
- Vermeer, J. Girl with a Pearl Earring. https://www.mauritshuis.nl/ en/explore/the-collection/artworks/girl-with-a-pearl-earring-670/. (1665).
- 46. Zhan, Q. Cylindrical vector beams: from mathematical concepts to applications. *Adv. Opt. Photonics* **1**, 1 (2009).
- Liu, M. et al. Broadband generation of perfect Poincare beams via dielectric spin-multiplexed metasurface. *Nat. Commun.* 12, 2230 (2021).
- Bao, Y., Ni, J. & Qiu, C. W. A minimalist single-layer metasurface for arbitrary and full control of vector vortex beams. Adv. Mater. 32, 1905659 (2019).
- Wang, Z.-Y. et al. Vectorial liquid-crystal holography. eLight 4, 5 (2024).
- 50. Slussarenko, S. et al. Guiding light via geometric phases. *Nat. Photonics* **10**, 571–575 (2016).
- Damodaran, A. R. et al. Phase coexistence and electric-field control of toroidal order in oxide superlattices. *Nat. Mater.* 16, 1003–1009 (2017).
- 52. Lovšin, M. et al. Patterning of 2D second harmonic generation active arrays in ferroelectric nematic fluids. *Giant* **19**, 100315 (2024).
- 53. Zhu, Z. et al. Compensation-free high-dimensional free-space optical communication using turbulence-resilient vector beams. *Nat. Commun.* **12**, 1666 (2021).
- 54. Li, H., Liu, H. & Chen, X. Dual waveband generator of perfect vector beams. *Photonics Res* **7**, 1340 (2019).
- 55. Li, H., Liu, H., Yang, Y., Lu, R. & Chen, X. Ultraviolet waveband vector beams generation assisted by the nonlinear frequency conversion. *Appl. Phys. Lett.* **119**, 011104 (2021).
- Li, H., Liu, H., Yang, Y., Lu, R. & Chen, X. Nonlinear generation of perfect vector beams in ultraviolet wavebands. *Chin. Phys. Lett.* 39, 034201 (2022).

- Chen, R., Agarwal, K., Sheppard, C. J. R. & Chen, X. Imaging using cylindrical vector beams in a high-numerical-aperture microscopy system. Opt. Lett. 38, 3111 (2013).
- 58. Hnatovsky, C., Shvedov, V. G. & Krolikowski, W. The role of light-induced nanostructures in femtosecond laser micromachining with vector and scalar pulses. *Opt. Express* **21**, 12651 (2013).
- 59. Chigrinov, V. et al. Diffusion model of photoaligning in azo-dye layers. *Phys. Rev. E* **69**, 061713 (2004).
- 60. Wu, H. et al. Arbitrary photo-patterning in liquid crystal alignments using DMD based lithography system. *Opt. Express* **20**, 16684–16689 (2012).

Acknowledgements

Reproduction of the Nanjing University logo achieved through patterned polar LCs. The use of the Nanjing University logo is granted with permission from Nanjing University. Copyright © Nanjing University. All rights reserved. This work is supported by the National Key Research and Development Program of China (No. 2022YFA1405000 (Y.-Q.L, L.-L.M., S.A.)); National Natural Science Foundation of China (Nos. T2488302 (Y.-Q.L), No. 62375119 (L.-L.M), and No. 62175102 (Y.Wang)); Natural Science Foundation of Jiangsu Province (Nos. BK20243067 (Y.-Q.L, L.-L.M), BK20250164 (L.-L.M.), and BK20232040 (L.-L.M)); National Science Fund for Excellent Young Scholars of China (No. T2422008 (S.A.)); the Research Fund for International Excellent Young Scientists (RFIS-II; No. 1231101194 (S.A.)); Natural Science Foundation of Guangdong Province (No. 2024B1515040023 (S.A.) and No. 2024A1515011313 (S.A.)); Science and Technology Projects in Guangzhou (No. SL2024A04J00994 (S.A.)); Fundamental Research Funds for the Central Universities (Nos. 2024300360 and 2025300215 (L.-L.M)). S.A. also thanks the support from the TCL Young Talents program.

Author contributions

L.-L.M., Y.-Q.L., and S.A. supervised the project. L.-L.M., Y.-Q.L., S.A., and G.-Y.Z. conceived the idea and designed the experiments. G.-Y.Z., L.-L.M., Y.Y., J.-T.P., J.Y., M.D., and N.W. performed the experiments, including material synthesis, measurements and analyses of material, structure, and optical properties. G.-Y.Z., L.-L.M., and Y.-Q.L. developed theoretical models for nonlinear optics and carried out the numerical calculation. E.L. and S.A. conducted numerical simulations of orientational fields based on an extended mean-field model. L.-L.M., G.-Y.Z., S.A., Y.-Q.L., and Y.Wang wrote the manuscript with the input from all authors. L.-L.M., G.-Y.Z., Y.Wang, S.A., Y.-Q.L., E.L., Z.-Y.W., J.-T.P., J.Y., M.D., Y.Wei, Y.Y., and N.W. discussed the results and proofread the manuscript.

Competing interests

The authors declare no competing interests.

Additional information

Supplementary information The online version contains supplementary material available at https://doi.org/10.1038/s41467-025-64463-2.

Correspondence and requests for materials should be addressed to Ling-Ling Ma, Yu Wang, Satoshi Aya or Yan-Qing Lu.

Peer review information *Nature Communications* thanks the anonymous reviewers for their contribution to the peer review of this work. A peer review file is available.

Reprints and permissions information is available at http://www.nature.com/reprints

Publisher's note Springer Nature remains neutral with regard to jurisdictional claims in published maps and institutional affiliations.

Open Access This article is licensed under a Creative Commons Attribution-NonCommercial-NoDerivatives 4.0 International License, which permits any non-commercial use, sharing, distribution and reproduction in any medium or format, as long as you give appropriate credit to the original author(s) and the source, provide a link to the Creative Commons licence, and indicate if you modified the licensed material. You do not have permission under this licence to share adapted material derived from this article or parts of it. The images or other third party material in this article are included in the article's Creative Commons licence, unless indicated otherwise in a credit line to the material. If material is not included in the article's Creative Commons licence and your intended use is not permitted by statutory regulation or exceeds the permitted use, you will need to obtain permission directly from the copyright holder. To view a copy of this licence, visit https://creativecommons.org/licenses/by-nc-nd/4.0/.

© The Author(s) 2025